




Circumventing huge volume strain in alloy anodes of lithium batteries

Hongyi Li ¹, Takitaro Yamaguchi², Shingo Matsumoto², Hiroaki Hoshikawa³, Toshiaki Kumagai³, Norihiko L. Okamoto ¹ & Tetsu Ichitsubo ¹ 

Since the launch of lithium-ion batteries, elements (such as silicon, tin, or aluminum) that can be alloyed with lithium have been expected as anode materials, owing to larger capacity. However, their successful application has not been accomplished because of drastic structural degradation caused by cyclic large volume change during battery reactions. To prolong lifetime of alloy anodes, we must circumvent the huge volume strain accompanied by insertion/extraction of lithium. Here we report that by using aluminum-foil anodes, the volume expansion during lithiation can be confined to the normal direction to the foil and, consequently, the electrode cyclability can be markedly enhanced. Such a unidirectional volume-strain circumvention requires an appropriate hardness of the matrix and a certain tolerance to off-stoichiometry of the resulting intermetallic compound, which drive interdiffusion of matrix component and lithium along the normal-plane direction. This metallurgical concept would invoke a paradigm shift to future alloy-anode battery technologies.

¹Institute for Materials Research, Tohoku University, Sendai 980-8577, Japan. ²Advanced Materials Development Laboratory, Sumitomo Chemical Co., Ltd., Tsukuba 300-3294, Japan. ³Energy and Functional Materials Research Laboratory, Sumitomo Chemical Co., Ltd., Ehime 792-8521, Japan.
✉email: tichi@imr.tohoku.ac.jp

Rechargeable batteries are indispensable devices in modern society and they are continuously improved toward higher energy density and longer lifetime^{1,2}. In lithium-ion batteries (LIBs) as a representative rechargeable battery, the combination of intercalation-type transition-metal-oxide cathode and carbonaceous anode materials have achieved a great success and win the current energy-storage device market^{3–5}. However, as the energy density of conventional LIBs have gradually reached the theoretical limit, further approaches are necessary for developing superior batteries^{6,7}. As a promising approach, high-capacity alloy-anode materials, such as Si, Sn, or Al, had been expected for the practical applications in advanced lithium batteries because of their much (three to ten times) higher capacities than a conventional graphite anode^{6,8–11}. Compared with the intercalation-type graphite anode^{12,13}, the alloy anodes must suffer large volume change during battery reactions^{11,14,15}, e.g., +300% volume expansion (increase) from Si to Li₂₁Si₅ (~4000 mAh g_{Si}⁻¹), +250% from Sn to Li₂₂Sn₅ (~990 mAh g_{Sn}⁻¹), and +100% from Al to AlLi (~990 mAh g_{Al}⁻¹), compared with +10% volume expansion from C₆ to LiC₆ (372 mAh g_C⁻¹). Such a huge volume change accompanied by lithiation or delithiation is substantially isotropic and causes critical irreversible damage to the matrix, which would consequently be fragmented into inactive fine powder drifting in the electrolyte^{16–18}. Therefore, if a metallic foil (especially, Sn or Al) could maintain a stable electrode structure during battery reactions, a heavy Cu current collector currently used would have been unnecessary, which would have benefited a remarkable increase of practical anode capacity. However, the application of alloy anodes has never been succeeded yet. One of effective approaches to avoid this pulverization problem is to downsize particles of active material and/or to fabricate porous electrode morphology, by which the volume change can be tolerated owing to the voids between the particles^{19–26}. However, the active materials must be prepared with supporting substances, such as in the form of composite electrode^{27–29} or attaching on nanostructures^{30–35}. Preparation of such supporting materials usually makes the manufacturing process complicated and decreases the practical anode capacity, which has impeded the development of alloy anodes.

Nevertheless, application of alloy anodes is still strongly demanded for easy-to-manufacture strategy of large-scale LIBs. In this work, to establish a concept of “one-material electrode,” which combines active material and collector, we show an innovative way of how to circumvent such a huge volume strain by utilizing metallurgical viewpoints such as thermodynamics, elastic strain, and diffusion. By examining structural stabilities of various metallic-foil electrodes during lithiation, we demonstrate that Al foil with appropriate hardness can be used as a self-standing anode for lithium batteries. An appropriate hardness of the matrix and a certain tolerance to off-stoichiometry of the resulting intermetallic compound can drive a two-dimensionally (in-plane) homogeneous lithiation reaction and one-dimensional (out-of-plane) interdiffusion to hold the Gibbs–Duhem relation, which effectively circumvent the volume-strain influences during battery reaction and the fatal pulverization problem of alloy anodes.

Results

Morphology after initial lithiation into various metals. To examine the structural stability of metal foil anodes, Al, Zn, and Sn foils were lithiated in coin-type cells with a Li counter-electrode, in which the electrolyte consisting of 1 M LiPF₆ and Ethylene Carbonate (EC) : Dimethyl Carbonate (DMC) in an equivolume ratio (50:50) was used for all the electrochemical tests. In general, the hardness of materials should largely affect the structural stability after lithiation. Thus, as to Al foils, we prepared three types of samples with different hardness, by

modifying purity and controlling conditions of rolling and heat treatment. Vickers hardness (HV) of each foil is shown in Fig. 1a. The foils were lithiated to a cathodic charge of 5 mAh cm⁻² at the current density of 0.5 mA cm⁻². As shown in Fig. 1a, the lithiated foils have distinctively different appearances.

First, it is interesting to note that soft metals less than HV 30, Sn (purity 99.9%) foil, and annealed 4N-Al foil (purity 99.99%, hereafter termed as “Al4N-HT”), are locally deformed plastically after lithiation. Undulation of the matrix, which is formed by alloying with Li on the front side (facing a Li-metal counter-electrode), is spread out the whole matrix. Besides, the lithiation occurs inhomogeneously, which indicates that the mechanical (elastic/plastic) deformation of matrix strongly affects the lithiation process. In contrast to the soft foils, hard as-rolled 2N-Al foil (purity 99.8%) shows very different lithiation behavior. On the front side, protruding AlLi grains are cracked (the phase identification is later shown in Fig. 2c), which suggests that the growing AlLi alloy could not deform the Al matrix but was contrary crushed by the hard Al matrix. Whereas dimple patterns are observed on the back side, suggesting that ductile fracture occurs due to the large tensile stress caused by the protruding AlLi grains on the front side. The morphology details are shown in Supplementary Fig. 1a.

Most importantly and surprisingly, the as-rolled 4N-Al foil (purity 99.99%, referred to as “Al4N-AR”) achieves homogeneous lithiation on the front side and no-damaged Al matrix remains on the back side. Thus, it seems that an appropriate hardness of matrix would prevent the deformation of anode matrix and the fracture of alloy phase; in the case of Al/AlLi, the most suitable hardness is eventually found to be ca. HV 35. The fact that there is no apparent plastic deformation in the matrix means that the volume expansion during lithiation occurs in the normal (i.e., out-of-plane) direction, i.e., unidirectional growth of the lithiated phase is driven. In contrast, although as-rolled Zn (purity 99.9%) has a similar matrix hardness to Al4N-AR, Li is almost deposited on the surface of Zn foil rather than forming a Zn-Li alloy. This difference would be attributed to the diffusivity of Li in Zn and the activation energy of lithiation, etc.^{36,37}. With a detailed explanation in Supplementary Note 1, scanning electron microscopy (SEM) images corresponding to Fig. 1 are given in Supplementary Fig. 1 and the potential profiles are shown in Supplementary Fig. 2 for comparison.

Attainment of homogeneous and unidirectional lithiation. To understand the differences in the degree of homogeneity on lithiation reaction and in characteristic feature of volume expansion, we observed the morphology changes accompanied by Li insertion and extraction, the results of which are summarized in Fig. 2a–h. Figure 2a shows field-emission SEM (FE-SEM) images of Al4N-AR in the lithiation process (I, II, and III) and delithiation after lithiation (IV), and Fig. 2f shows those of Al4N-HT as well. In the early stage (I–II) of lithiation, AlLi phase forms on the surface and causes the protrusions due to the volume expansion (about 100% increase for Al to AlLi). As found from the energy dispersive X-ray spectroscopy (EDX) mappings, the intensity of Al K α is significantly reduced at the protrusions; as Li element cannot be detected by EDX, the intensity decrease of Al K α directly indicates a higher Li composition in such protruded regions, corresponding to the AlLi formation. It deserves to note that grain sizes of AlLi are quite different between the two cases. As found from the electron backscatter diffraction (EBSD) patterns in Fig. 2a, f, the crystalline size in Al4N-AR is far smaller than that in Al4N-HT; thus, it seems that the grain size of AlLi in

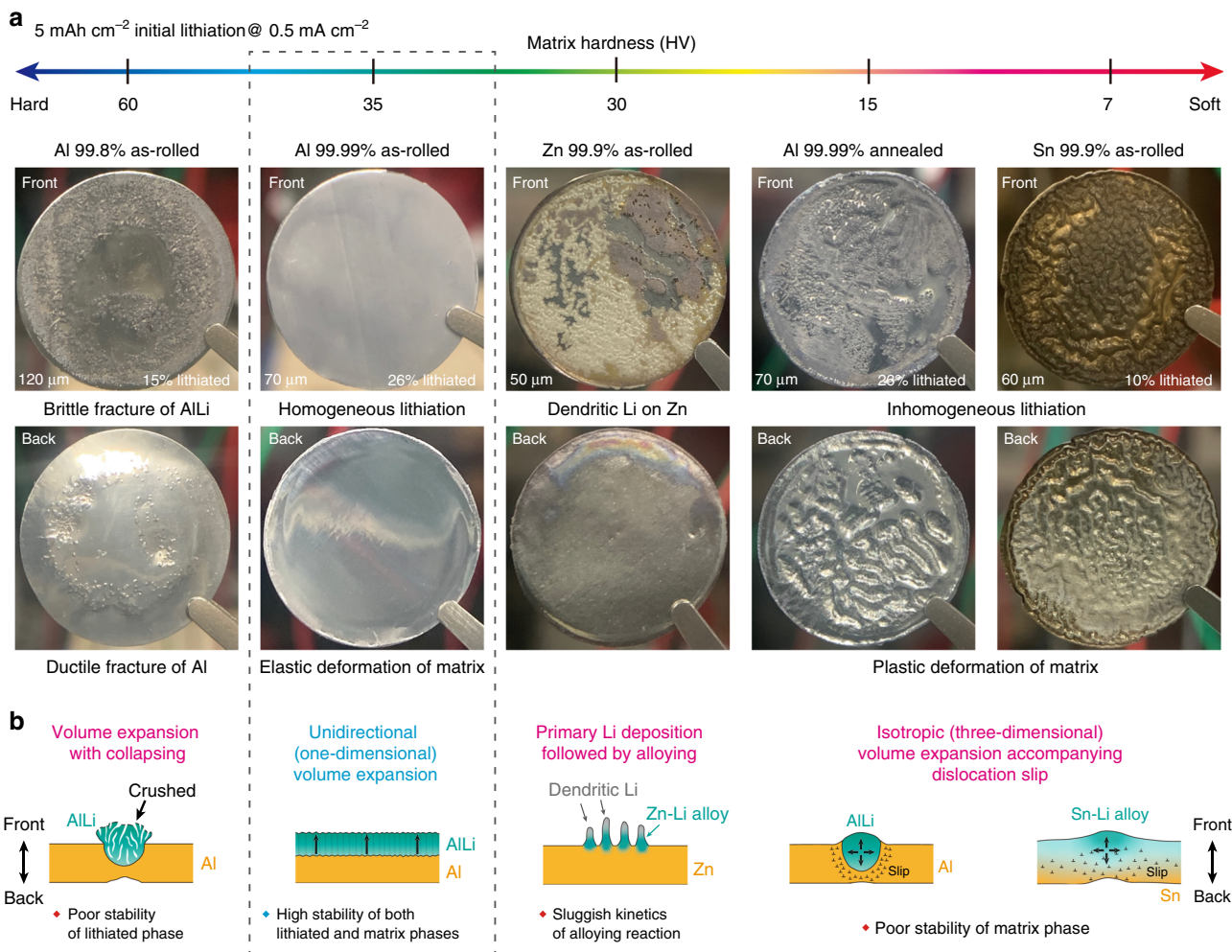


Fig. 1 Structural stability of various metallic foils after initial lithiation. **a** Photographs of various metallic foils after lithiation of 5 mAh cm⁻². Average Vickers hardness (HV) of each foil is given in the upper graph. The lithiation was conducted at a current density of 0.5 mA cm⁻² with a Li metal counter-electrode. The original thickness and lithiation percentage of each foil are also denoted in the front-side photo. The percentage figure of lithiation in each sample is displayed based on the total capacity of each anode depending on the foil thickness. As to Zn, the percentage is not presented, because Li metal is mainly deposited on the surface instead of the formation of Li-Zn alloy; see also Supplementary Fig. 1c. The as-rolled Al (99.99%) foil shows a homogeneous lithiation on the front side and a sufficiently retained stable Al matrix on the back side. **b** Schematic illustrations of lithiation process reasonably inferred from SEM pictures obtained for respective foils; see Supplementary Fig. 1.

each foil may reflect the crystalline size in each in the early stage of lithiation. Comparing the EDX mappings for Al4N-AR and Al4N-HT, one can find that there are light-colored areas (gray) around the protrusions (black) in Al4N-HT, but there is no such area in Al4N-AR. This indicates that, for the soft Al4N-HT matrix, lithiated regions can also grow locally starting from the protruded AlLi grains, which is strongly supported by the occurrence of large amount of dislocation slip lines observed in the SEM images.

In the further lithiation (from II to III in Fig. 2a, f), the two samples show a crucial difference in morphology. In Al4N-AR, fine AlLi particles are uniformly formed all over the surface, i.e., the homogeneous lithiation is successfully attained. On the other hand, in Al4N-HT, the AlLi phase grows preferentially from the already swelled regions by lithiation, where the Al matrix is plastically deformed with a large amount of slips. Figure 2b, c show the cross-section SEM images of Al4N-AR before and after lithiation, respectively. It is noteworthy that the very flat interface of AlLi proceeds along the depth direction from the front (i.e., facing the Li electrode) to the back side and,

simultaneously, the front surface goes up to increase the foil thickness. The thickness of the lithiated layer (~80 μm) is about twice that of the initial foil (~40 μm), i.e., almost of volume expansion caused by the Al-to-AlLi transformation is realized only along the out-of-plane direction. Furthermore, by comparing Fig. 2a(II) and 2a(III), one can find that the current density would affect the nucleation frequency on the Al surface, in that a large number of AlLi protrusions are formed in (III) at 0.5 mA cm⁻² compared with (II) at 0.05 mA cm⁻². The unidirectional volume expansion, however, would not be affected by the current density unless the operating potential reaches the redox potential of Li⁺/Li. Figure 2d shows that the X-ray diffraction (XRD) pattern of the 53% lithiated Al4N-AR foil is in good agreement with the standard data of AlLi crystal in the inorganic crystal structure database (ICSD). In extracting Li from the lithiated Al4N-AR foil (from III to IV in Fig. 2a), the Al matrix is self-organized to form a columnar structure with cleavages and micropores following the dealloying porous mechanism²⁴, whereas in Al4N-HT foil (from III to IV in Fig. 2f), pulverization proceeds with delithiation, starting from the AlLi

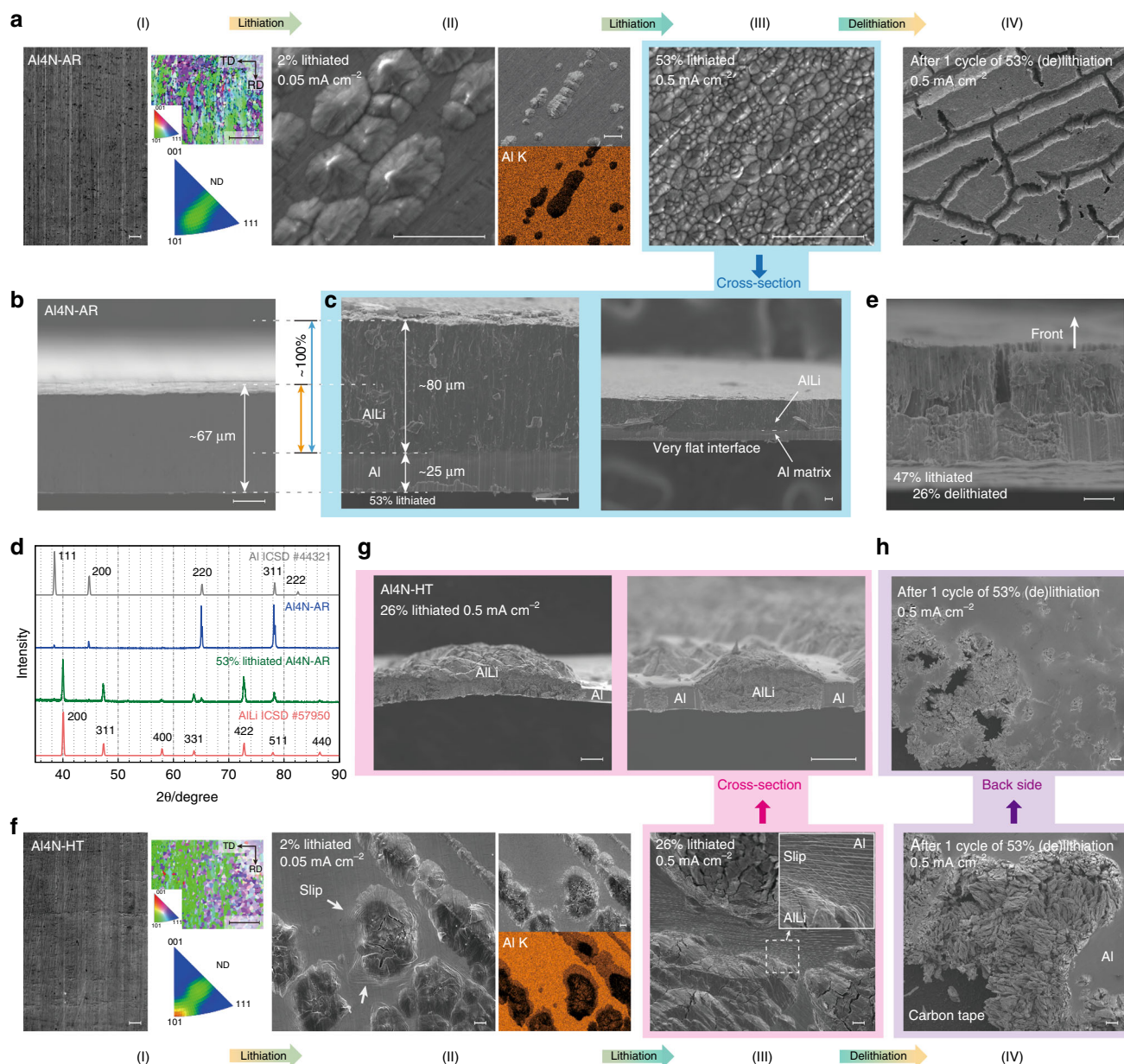


Fig. 2 Lithiation-delithiation processes of Al4N-AR (purity 99.99%, as-rolled Al) foil and Al4N-HT (purity 99.99%, well-annealed Al) foil.

a Morphology changes (I, II, III, and IV) on the front side (facing the Li electrode) of Al4N-AR during lithiation and delithiation, and EBSD pattern of the initial state. Al4N-AR shows a homogenous lithiation and maintains a stubborn Al-matrix layer with a good structure stability. **b** Cross-section of a bare Al4N-AR foil. **c** Cross-section of a 53%-lithiated Al4N-AR foil. A very flat interface is observed between lithiated phase and Al matrix. The lithiated layer becomes twice thick, suggesting that the volume expansion occurs along the direction normal to the Al foil (i.e., one-dimensionally). **d** XRD profiles obtained in the reflection geometry for the Al4N-AR foil before and after lithiation. **e** Cross-section of an Al4N-AR foil that has undergone 47% lithiation and subsequent 26% delithiation. Al matrix is self-organized to form a columnar structure during delithiation. **f** Morphology changes (I, II, III, and IV) on the front side of Al4N-HT during lithiation and delithiation, and EBSD pattern of the initial state. The AlLi grains are inhomogeneously formed, resulting in the pulverization during delithiation. **g** Cross-section of a 26% lithiated Al4N-HT foil, where the AlLi phase penetrates the foil accompanied with plastic deformation. **h** Backside view of an Al4N-HT foil that has undergone a 53% lithiation and delithiation cycle. The foil is pulverized during delithiation. Scale bars in SEM images are 20 μm for **a-f** and 100 μm for **g, h**. EBSD patterns of Al matrices inset in **a** and **f** indicate a marked grain growth in the recrystallization of Al4N-AR and Al4N-HT, respectively. The percentage figures of lithiation are displayed based on the total capacity of the Al foil.

grains that have precedingly reached the back side of the foil, as shown in Fig. 2g, h.

Mechanism from metallurgical insight. To realize the unidirectional AlLi formation that is capable of circumventing huge volume strain, the Al element of matrix component must flow

from inside to the surface during lithiation. Otherwise, the volume strain is inevitably caused by the Li compound formation, which results in significant deterioration of electrodes. Here, based on the viewpoints of thermodynamics, elasticity, and atomic diffusion, we consider the reason why such a unidirectional AlLi formation can be driven. Figure 3a illustrates schematically the Gibbs free-energy profiles in Al-Li binary system, in

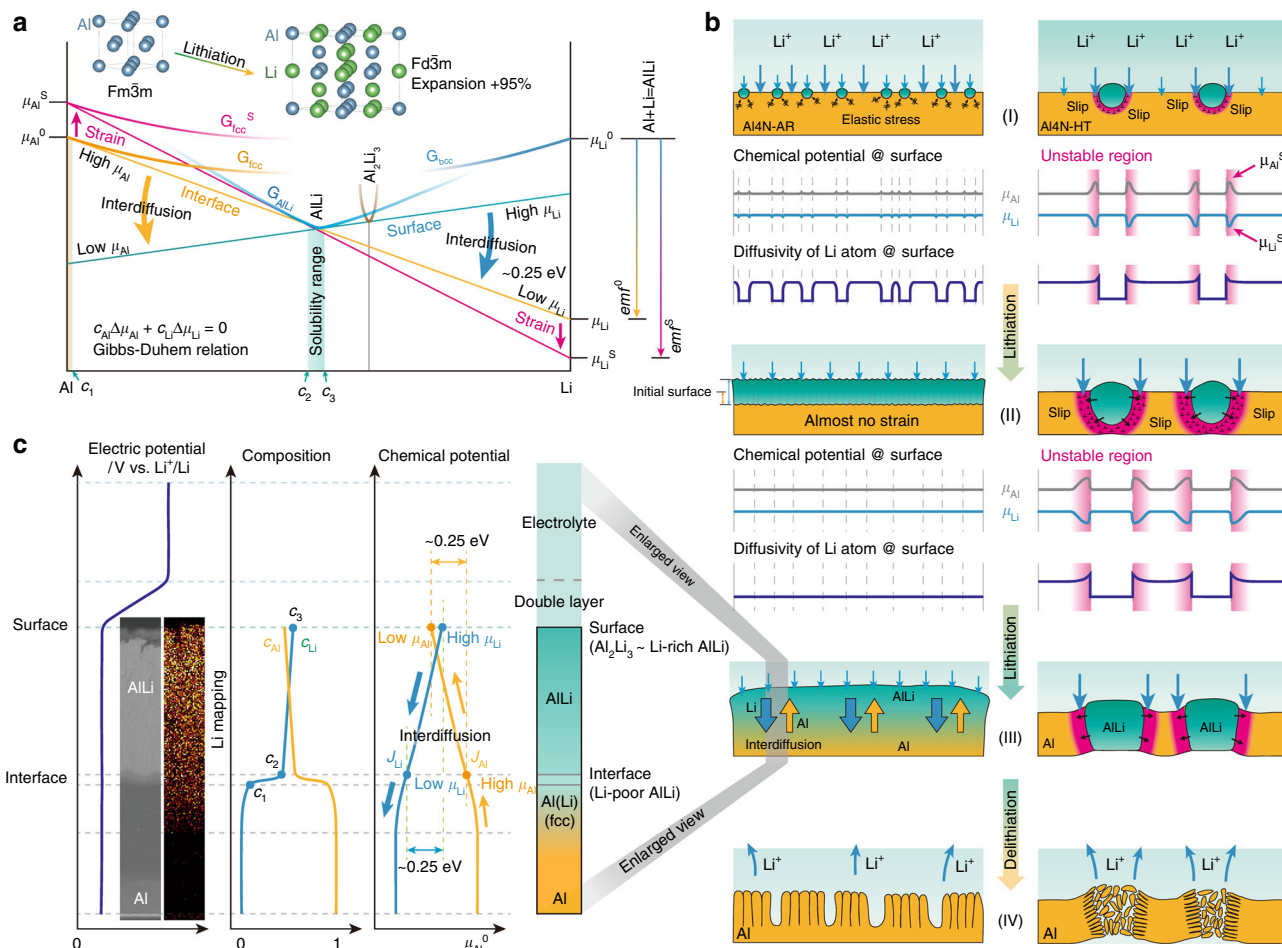


Fig. 3 Lithiation mechanism on an Al anode. **a** The Gibbs free-energy curves in Al-Li binary system. The two-phase reaction of fcc-Al/ $\text{AlLi}_{\text{Li-poor}}$ (whose Li composition is C_2) occurs during lithiation. The chemical driving force of fcc-Al/ AlLi reaction ($-\text{emf}^0$) is about 0.38 eV (yellow line), but the value is enhanced when certain amount of strain energy is accumulated by mechanical deformation (pink line). Basically, the consideration of local equilibrium of fcc-Al/ $\text{AlLi}_{\text{Li-poor}}$ is sufficient, but around the surface that of $\text{AlLi}_{\text{Li-rich}}/\text{Al}_2\text{Li}_3$ is also needed during lithiation. **b** Schematic illustration of the lithiation processes of mechanically hard and soft Al foils; (left) Al4N-AR and (right) Al4N-HT. Stages (I, II, III, and IV) corresponds to the SEM images in Fig. 2a; see also Supplementary Fig. 3. The appropriate hardness of Al4N-AR enables the homogeneous lithiation. As the diffusivity in the AlLi phase possessing an ordered lattice is generally slower than that in the fcc Al phase, the formation of AlLi in the remaining Al matrix is kinetically preferential, whereas the already deformed Al matrix tends to be preferentially attacked by Li thermodynamically. **c** Schematic profiles of gradients of electric potential, composition, and chemical potentials of Li and Al to illustrate the unidirectional volume-expansion mechanism during lithiation on Al4N-AR. Insets show the SEM image and SIMS mapping of Li at the ion-beam-fabricated cross-section of a partially lithiated Al4N-AR; full field images are given in Supplementary Fig. 4. The chemical-potential gradients of Li and Al due to those of respective compositions drives the interdiffusion of Al and Li, whose maximum driving force is estimated to be about 0.25 eV.

which the free-energy curves, G_{fcc} , G_{bcc} , and G_{AlLi} are semi-quantitatively drawn based on the thermodynamic database (fcc: Al solid solution, bcc: Li solid solution)³⁸. According to the Al-Li phase diagram, the insertion of Li into Al matrix undergoes a two-phase reaction of fcc-Al/ AlLi phases, where each chemical potential in the fcc Al solid solution and AlLi phase must be equal at equilibrium state; μ_{Li} in fccAl = μ_{Li} in AlLi and μ_{Al} in fccAl = μ_{Al} in AlLi as indicated by yellow line in Fig. 3a. The chemical-potential difference of Li between AlLi phase and pure Li phase determines the electromotive force (emf^0) in Fig. 3a) of the lithiation reaction, $\text{Al} + \text{Li} = \text{AlLi}$. What we want to discuss here are the following two points: (i) in-plane homogeneous reaction of Li on the surface and (ii) transfer of Al toward the surface.

Let us first address the term (i). Difference in matrix hardness yields different strain effects during the Li compound formation. When plastic deformation of the Al matrix occurs, large amount of dislocations are introduced into the matrix, so that the Gibbs free energy of the deformed Al matrix is increased, as indicated

by the G_{fcc}^S in Fig. 3a. Then, according to the Gibbs-Duhem relation, $c_{\text{Al}}d\mu_{\text{Al}} + c_{\text{Li}}d\mu_{\text{Li}} = 0$, a two-phase equilibrium state must be shifted, as shown by a pink line in Fig. 3a. Consequently, the chemical potential of Li is apparently lowered and the electromotive force is enhanced more or less. This effect would be a main reason for the inhomogeneous lithiation in the softer Al4N-HT electrode. As soft Al matrix in the Al4N-HT electrode cannot bear the internal stress caused from the electrochemically growing AlLi phase, the volume expansion induces plastic deformation of the matrix. Afterwards, Li would prefer to be inserted into such unstable regions to obtain a chemical-potential gain. In addition, the plastic deformation involves a large amount of lattice defects, which would facilitate the Li diffusion in Al matrix. As illustrated in Fig. 3b (right), these thermodynamic and kinetic effects can work synergistically and the formation of AlLi easily reaches the back side, which leads to fracture and pulverization of electrode upon delithiation. On the contrary, as shown in the Al4N-AR foil in Fig. 1, appropriate hardness of the matrix can circumvent

plastic deformation of the matrix, i.e., Li compound cannot deform the matrix. In this case, the growth of AlLi would be retarded due to the elastic stress in the Al matrix¹⁷. Furthermore, unlike the case of softer matrix, no preferential region for Li insertion exists in the appropriately hard matrix, so that the lithiation can evenly occur in the remaining Al matrix on the surface, resulting in the homogenous reaction in plane.

Next, we consider the term (ii) why unidirectional diffusion from the inside to surface of the Al matrix component is driven after homogeneous lithiation on the surface is completed. The inset of Fig. 3c shows SEM image and corresponding Li element mapping for the cross-section of a lithiated Al4N-AR foil, which was prepared by focused ion beam (FIB) and measured by time-of-flight secondary ion mass spectrometry (TOF-SIMS). Interestingly, it is found that Li composition in the AlLi phase slightly decreases from the surface to the inside. As the AlLi phase tolerates off-stoichiometric composition according to the Al-Li phase diagram, the composition gradient can be allowed in the AlLi single phase. Again, revisiting the Gibbs–Duhem relation, not only the chemical potential of Li but also that of Al is changed gradually, as shown in Fig. 3c; μ_{Al} increases, whereas μ_{Li} decreases from the surface toward inside. The chemical-potential difference between the surface and inside is estimated to be about 0.25 eV for each element based on the thermodynamic database³⁸. This chemical-potential gradient of each element drives the interdiffusion, $\mathbf{J}_{\text{Al}} = -M_{\text{Al}} \text{grad } \mu_{\text{Al}}$ and $\mathbf{J}_{\text{Li}} = -M_{\text{Li}} \text{grad } \mu_{\text{Li}}$, where M_{Al} and M_{Li} are the mobilities of respective elements; thereby, Al element flows from the inside to surface, whereas Li element flows from the surface to inside. Consequently, the Al/AlLi interface gradually moves toward the inside of the Al matrix,

whereas the AlLi front surface grows toward the counter-electrode side with moving the surface. This one-dimensional interdiffusion mechanism can circumvent the huge volume strain due to the lithiation. In contrast, we previously attempted to confine the volume expansion of Sn-Li alloy (most of the Sn-Li intermetallic compounds are line compounds) by embedding Sn in unidirectional porous Cu³⁹, but lithiation occurred only on the Sn surface without further infiltration of Li into the Sn matrix. Thus, it is reasonably inferred that a certain tolerance to off-stoichiometry of Li intermetallic compounds is crucially important to yield the driving force of interdiffusion.

Practical application to alloy-anode lithium battery. Finally, we exemplify a concept of “one-material electrode” combining active material and collector using a practical collector-free Al anode for lithium batteries. Figure 4a compares the structure of an Al-anode lithium battery to that of a conventional LIB. An Al4N-AR foil is assembled as an anode instead of the conventional graphite composite; the remaining Al matrix layer, which is indispensable to maintain the stable structure of the electrode, can also play a role of current collector and a heavy Cu foil is not needed to be employed any longer in this type of electrode, which would markedly simplify the battery manufacturing process. As shown in Fig. 4b, an Al-foil anode is partially lithiated in the pre-charge (initial lithiation) process and when Li is inversely extracted from the lithiated layer in the first discharge (delithiation) process, the remaining Al matrix shrinks to form columnar structure with producing some internal pores. This columnar-porous structure of the active material, which can be formed in-operando in the initial lithiation/delithiation cycle, plays a significant role for later

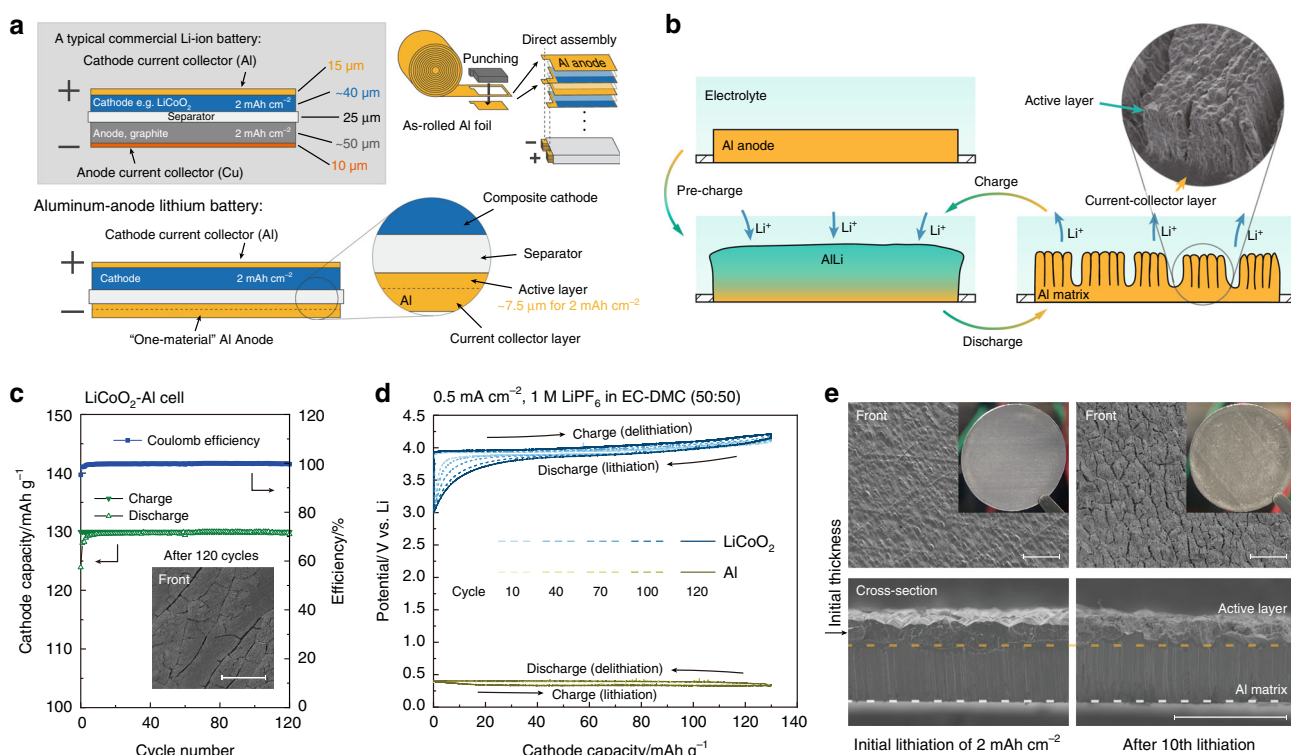


Fig. 4 Application and performance of an Al-anode lithium battery. **a** Structure of an Al-anode Li-ion battery compared with a conventional Li-ion battery. The Cu anode current collector is not needed when using the Al anode. The as-rolled Al anode can be assembled directly. **b** Electrode reaction of an Al anode. Al matrix is partly lithiated during pre-charge and the lithiated layer forms columnar-porous structure in discharge and works as the active materials in further cycles. **c** Cycle performance of a lithium battery consisting of an Al anode and a LiCoO₂ cathode. The inset SEM image shows the surface of the Al anode after 120 cycles. Electrode properties at initial cycles is shown in Supplementary Fig. 2e. **d** Potential profiles of cycle 10, 40, 70, 100 and 120 in the cycle tests. No obvious degradation is observed on the Al anode. **e** Surfaces and cross-sections of Al anodes after initial lithiation of 2 mAh cm⁻² and after subsequent 10th lithiation. The active layer and current-collector layer are well-retained without consuming. Scale bars in SEM images are 100 μm.

cyclic charge/discharge processes. Figure 4c, d show the battery performance of a LiCoO₂-Al cell; almost 100% Coulomb efficiency is retained and no obvious morphology change is observed after the 120th cycle. The potential-capacity profiles of the 10, 40, 70, 100, and 120th cycles are plotted in Fig. 4d, where the Al anode behaves a stable operating potential at 0.3–0.4 V vs. Li, although a slight degradation is observed on the LiCoO₂ cathode. To confirm whether the active Al layer is maintained or consumed to fragment out, we compared the cross-section morphologies of two samples obtained after the initial lithiation of 2 mAh cm⁻² and subsequent tenth lithiation. As shown in Fig. 4e, except a slight increase of internal spaces between the columns, the active layer substantially keeps as a bulk without fragmentation and no obvious difference is observed both in the thicknesses of active-material layer (higher part of the Al electrode) and current-collector layer (lower part of the Al electrode).

Discussion

In the present work, the hardness of metallic foil is considered as a key parameter to balance the strengths between matrix and lithiated phase. If the strengths of both phases are comparable to each other, the high structure stability can be maintained during the first lithiation as in the case of Al₄N-AR. This is because the resultant lithiated phase (Alli) cannot deform the Al matrix and, therefore, the chemical potential of Al remains unchanged everywhere in the Al matrix. However, if there are locally deformed regions in the Al matrix, where the Al chemical potential is high (see the pink line in Fig. 3a), Li atoms preferentially attack and annihilate such unstable regions (as shown experimentally in Fig. 2f, g). Thus, the local strain induces the inhomogeneous reaction of Li with the anode material. Consequently, it is very important that the Al matrix is not deformed by the Alli formation. Next, it is indispensable to drive the Al diffusion from matrix toward surface (interface between electrolyte/anode) to circumvent the internal volume expansion. Fortunately, it is possible for Al, because the Alli compound tolerates the off-stoichiometric composition, so that the composition gradient can be formed in the Alli compound. The Li composition around the surface is higher than that in the inner matrix, i.e., the Al composition is lower around the surface. Thus, the Al diffusion toward the surface can be successfully driven. Consequently, the volume expansion with lithiation is confined only to the normal direction. In terms of the tolerance of off-stoichiometric composition, Al metal is more suitable for the alloy-anode material than other elements that show stoichiometric composition in the Li compounds. However, it would be effective to add a third element for obtaining off-stoichiometric characteristics due to a certain entropy effect.

Owing to the homogenous lithiation and unidirectional volume-strain circumvention, a very flat interface is formed between lithiated phase and Al matrix (see Figs. 2c and 4e), which conceptually divides a partly lithiated Al foil to an active-material layer and a current-collector layer. Thanks to this layered structure, the one-material Al anode is endowed with an excellent structural stability. Furthermore, as the active layer once lithiated would be self-organized to form a porous structure during delithiation, the expanded volume with extra space in the columnar-porous active-material layer can accommodate the volume expansion by the subsequent lithiation. This prevents the relatively fragile Alli from impinging with each other in further reactions and, therefore, circumvents the fatal pulverization in a similar mechanism as well as in a nanoporous silicon²⁴, leading to excellent cyclability of the one-material Al anode. Consequently, focusing on the active-material layer, it shows a large capacity close to the theoretical value of ~990 mAh g_{Al}⁻¹ and ~2680 mAh cm_{Al}⁻³ with quite a high cyclability. As shown in

Supplementary Note 2 and Supplementary Fig. 5, benefiting from the absence of a relatively heavy Cu current collector, this type of Al anode for lithium batteries can achieve a higher practical capacity than a conventional carbonaceous anode and even than a Li metal anode (with a Cu collector), which would lead to future safe and high-energy-density lithium batteries.

Methods

Materials preparation. Al foils used in the present study were produced by Sumitomo Chemical Co., Ltd. As-rolled and annealed Al foils of purity 99.99% and as-rolled Al foil of purity 99.8% were prepared from corresponding Al ingots. As-rolled Zn foil of 99.9% was purchased from The Nilaco Corporation and as-rolled Sn foil of 99.9% was purchased from Takeuchi Metal Foil and Powder Co., Ltd. The electrolyte of 1 M LiPF₆ in EC:DMC (50:50) solution was purchased from Sigma-Aldrich Co. LLC. LiCoO₂ powder was purchased from Toshiba Manufacturing Co., Ltd. Composite cathode was prepared by mixing the LiCoO₂ powder with conductive carbon black (Super C65) and polyvinylidene difluoride binder (5% dispersed in *N*-methylpyrrolidone, Kureha Corporation) in a weight ratio of 8:1:1. The mixture was pasted on a 20 μm-thick Al foil with an adjustable film applicator (BEVS Industrial Co., Ltd) and reached a mass loading of more than 15 mg cm⁻² of LiCoO₂. The pasted mixture was then dried in a vacuum dryer at 120 °C for 12 h to obtain a composite cathode sheet. Li metal foil used as the counter and reference electrodes was purchased from Honjo Metal Co., Ltd.

Electrochemical tests. Electrochemical tests were conducted by a potentiostat VMP-3 or VSP-300 (Bio-Logic SAS). Three-electrode coin-type cells (SB7, EC-frontier Co., Ltd) were assembled in glovebox filled with high-purity argon atmosphere. Working electrodes and counter electrodes had a round shape with a diameter of 16 mm. A Li metal rod with a diameter of 1 mm was used as a reference electrode. A polyethylene film or glass fiber filter was employed as the separator. The cell structure is shown in Supplementary Fig. 6.

Morphology observation. Samples were washed by dropping tetrahydrofuran (99.5%, FUJIFILM Wako Pure Chemical Corporation) and subsequently dried in argon atmosphere. Photos of samples were taken with an iPhone Xs Max (Apple, Inc.). Microstructures of the lithiated and delithiated samples (except the inset in Fig. 3c) were observed in detail with a FE-SEM JSM-7200F (JEOL Ltd). EBSD measurement was carried out for the Al foils with a detector (Symmetry, Oxford Instruments) attached on the FE-SEM. The samples were prepared in argon atmosphere and transferred to the high vacuum chamber of FE-SEM without exposure to air. Cross-section samples in Figs. 2 and 4 were prepared with a trimming cutter (C-4, WISTA Co., Ltd). The sample in the inset of Fig. 3c was prepared using FIB to obtain a perfect cross-section plane. The subsequent TOF-SIMS measurement of Li composition was entrusted to Sumika Chemical Analysis Service, Ltd.

Vickers hardness. Hardness of each metal foil was measured with a micro HV tester (HMV-G21DT, Shimadzu Corporation). A test force of HV0.05 (490.3 mN) was employed and hold for 15 s. More than six points were measured for each sample with appropriate intervals. The average hardness value was presented in Fig. 1.

X-ray diffraction. XRD patterns were measured using an automated multipurpose X-ray diffractometer SmartLab (Rigaku Corporation). For the lithiated sample, an air-tight stage was used to keep an argon atmosphere throughout the experiment without exposure to air.

Calculation of free energy. The Gibbs free energies of Al-Li binary phases shown in Fig. 3a were depicted schematically in the light of a computer calculation using the software of CaTCalc SE developed by National Institute of Advanced Industrial Science and Technology, Japan, with a thermodynamic database provided by National Institute for Materials Science, Japan.

Data availability

The data that support the findings of this study are available from the corresponding author upon request.

Received: 7 January 2020; Accepted: 12 March 2020;

Published online: 13 April 2020

References

1. Chu, S. & Majumdar, A. Opportunities and challenges for a sustainable energy future. *Nature* **488**, 294–303 (2012).

- Larcher, D. & Tarascon, J. M. Towards greener and more sustainable batteries for electrical energy storage. *Nat. Chem.* **7**, 19–29 (2015).
- Goodenough, J. B. & Park, K. S. The Li-ion rechargeable battery: a perspective. *J. Am. Chem. Soc.* **135**, 1167–1176 (2013).
- Whittingham, M. S. Lithium batteries and cathode materials. *Chem. Rev.* **104**, 4271–4302 (2004).
- Yoshino, A. The birth of the lithium-ion battery. *Angew. Chem. Int. Ed.* **51**, 5798–5800 (2012).
- Tarascon, J. M. & Armand, M. Issues and challenges facing rechargeable lithium batteries. *Nature* **414**, 359–367 (2001).
- Armand, M. & Tarascon, J. M. Building better batteries. *Nature* **451**, 652–657 (2008).
- Besenhard, J. O., Yang, J. & Winter, M. Will advanced lithium-alloy anodes have a chance in lithium-ion batteries? *J. Power Sources* **68**, 87–90 (1997).
- Hamon, Y. et al. Aluminum negative electrode in lithium ion batteries. *J. Power Sources* **97–98**, 185–187 (2001).
- Park, C. M., Kim, J. H., Kim, H. & Sohn, H. J. Li-alloy based anode materials for Li secondary batteries. *Chem. Soc. Rev.* **39**, 3115–3141 (2010).
- Obrovac, M. N. & Chevrier, V. L. Alloy negative electrodes for Li-ion batteries. *Chem. Rev.* **114**, 11444–11502 (2014).
- Fong, R., Vonsacken, U. & Dahn, J. R., Studies of lithium intercalation into carbons using nonaqueous electrochemical cells. *J. Electrochem. Soc.* **137**, 2009–2013 (1990).
- Dahn, J. R., Zheng, T., Liu, Y. & Xue, J. S. Mechanisms for lithium insertion in carbonaceous. *Mater. Sci.* **270**, 590–593 (1995).
- Winter, M. & Besenhard, J. O. Electrochemical lithiation of tin and tin-based intermetallics and composites. *Electrochim. Acta* **45**, 31–50 (1999).
- McDowell, M. T., Lee, S. W., Nix, W. D. & Cui, Y. 25th anniversary article: understanding the lithiation of silicon and other alloying anodes for lithium-ion batteries. *Adv. Mater.* **25**, 4966–4985 (2013).
- Hirai, K. et al. Effects of volume strain due to Li–Sn compound formation on electrode potential in lithium-ion batteries. *Acta Mater.* **56**, 1539–1545 (2008).
- Ichitsubo, T. et al. Influence of mechanical strain on the electrochemical lithiation of aluminum-based electrode materials. *J. Electrochem. Soc.* **159**, A14–A17 (2011).
- Liu, X. H. et al. Size-dependent fracture of silicon nanoparticles during lithiation. *ACS Nano* **6**, 1522–1531 (2012).
- Chan, C. K. et al. High-performance lithium battery anodes using silicon nanowires. *Nat. Nanotechnol.* **3**, 31–35 (2008).
- Yu, Y., Gu, L., Zhu, C., van Aken, P. A. & Maier, J. Tin nanoparticles encapsulated in porous multichannel carbon microtubes: preparation by single-nozzle electrospinning and application as anode material for high-performance Li-based batteries. *J. Am. Chem. Soc.* **131**, 15984–15985 (2009).
- Hertzberg, B., Alexeev, A. & Yushin, G. Deformations in Si–Li anodes upon electrochemical alloying in nano-confined space. *J. Am. Chem. Soc.* **132**, 8548–8549 (2010).
- Wu, H. et al. Stable cycling of double-walled silicon nanotube battery anodes through solid-electrolyte interphase control. *Nat. Nanotechnol.* **7**, 310–315 (2012).
- Wang, C. et al. Self-healing chemistry enables the stable operation of silicon microparticle anodes for high-energy lithium-ion batteries. *Nat. Chem.* **5**, 1042–1048 (2013).
- Wada, T. et al. Bulk-nanoporous-silicon negative electrode with extremely high cyclability for lithium-ion batteries prepared using a top-down process. *Nano Lett.* **14**, 4505–4510 (2014).
- Lin, D. et al. A high tap density secondary silicon particle anode fabricated by scalable mechanical pressing for lithium-ion batteries. *Energy Environ. Sci.* **8**, 2371–2376 (2015).
- An, Y. et al. Green, scalable, and controllable fabrication of nanoporous silicon from commercial alloy precursors for high-energy lithium-ion batteries. *ACS Nano* **12**, 4993–5002 (2018).
- Li, H. The crystal structural evolution of nano-Si anode caused by lithium insertion and extraction at room temperature. *Solid State Ion.* **135**, 181–191 (2000).
- Li, X., Dhanabalan, A., Gu, L. & Wang, C. Three-dimensional porous core-shell Sn@Carbon composite anodes for high-performance lithium-ion battery applications. *Adv. Energy Mater.* **2**, 238–244 (2012).
- Meschini, I. et al. High-performance Sn@carbon nanocomposite anode for lithium batteries. *J. Power Sources* **226**, 241–248 (2013).
- Kim, H. & Cho, J. Superior lithium electroactive mesoporous Si@Carbon core–shell nanowires for lithium battery anode material. *Nano Lett.* **8**, 3688–3691 (2008).
- Meduri, P., Pendyala, C., Kumar, V., Sumanasekera, G. U. & Sunkara, M. K. Hybrid tin oxide nanowires as stable and high capacity anodes for Li-ion batteries. *Nano Lett.* **9**, 612–616 (2009).
- Wu, H. & Cui, Y. Designing nanostructured Si anodes for high energy lithium ion batteries. *Nano Today* **7**, 414–429 (2012).
- Ji, J. et al. Graphene-encapsulated Si on ultrathin-graphite foam as anode for high capacity lithium-ion batteries. *Adv. Mater.* **25**, 4673–4677 (2013).
- Liu, Y., Zhang, N., Jiao, L., Tao, Z. & Chen, J. Ultrasmall Sn nanoparticles embedded in carbon as high-performance anode for sodium-ion batteries. *Adv. Funct. Mater.* **25**, 214–220 (2015).
- Qin, J. et al. Graphene networks anchored with Sn@graphene as lithium ion battery anode. *ACS Nano* **8**, 1728–1738 (2014).
- Wang, J., King, P. & Huggins, R. Investigations of binary lithium-zinc, lithium-cadmium and lithium-lead alloys as negative electrodes in organic solvent-based electrolyte. *Solid State Ion.* **20**, 185–189 (1986).
- Chen, C., Yang, Y. & Shao, H. Enhancement of the lithium cycling capability using Li–Zn alloy substrate for lithium metal batteries. *Electrochim. Acta* **137**, 476–483 (2014).
- Hallstedt, B. & Kim, O. Thermodynamic assessment of the Al–Li system. *Int. J. Mater. Res.* **98**, 961–969 (2007).
- Ichitsubo, T. et al. Mechanical-energy influences to electrochemical phenomena in lithium-ion batteries. *J. Mater. Chem.* **21**, 2701–2708 (2011).

Acknowledgements

This work is a joint research project contracted between Tohoku University and Sumitomo Chemical Co. Ltd. This work is partly supported by Grant-in-Aid for Scientific Research (S) number 18H05249 and Grant-in-Aid for JSPS Research Fellow number 18J11696 commissioned by Japan Society for the Promotion of Science (JSPS).

Author contributions

T.I. and T.Y. conceived the study. H.L. designed the research plan and conducted the main part of experiments. H.H. and T.K. prepared the Al samples. S.M. conducted analysis of the Li distribution in Al samples. N.L.O. and H.L. conducted the EBSD measurements. H.L. and T.I. wrote the manuscript. All authors discussed the results and contributed to the manuscript.

Competing interests

T.Y., S.M., H.H., and T.K. are employees of Sumitomo Chemical Co., Ltd. The other authors declare no competing interests.

Additional information


Supplementary information is available for this paper at <https://doi.org/10.1038/s41467-020-15452-0>.

Correspondence and requests for materials should be addressed to T.I.

Peer review information *Nature Communications* thanks the anonymous reviewer(s) for their contribution to the peer review of this work.

Reprints and permission information is available at <http://www.nature.com/reprints>

Publisher's note Springer Nature remains neutral with regard to jurisdictional claims in published maps and institutional affiliations.

 **Open Access** This article is licensed under a Creative Commons Attribution 4.0 International License, which permits use, sharing, adaptation, distribution and reproduction in any medium or format, as long as you give appropriate credit to the original author(s) and the source, provide a link to the Creative Commons license, and indicate if changes were made. The images or other third party material in this article are included in the article's Creative Commons license, unless indicated otherwise in a credit line to the material. If material is not included in the article's Creative Commons license and your intended use is not permitted by statutory regulation or exceeds the permitted use, you will need to obtain permission directly from the copyright holder. To view a copy of this license, visit <http://creativecommons.org/licenses/by/4.0/>.

© The Author(s) 2020